Anisotropic adaptive nearly body-fitted meshes for CFD

Dieu-Linh Quan[1], Thomas Toulorge, Gaëtan Bricteux, Jean-François Remacle, Emilie Marchandise

Université catholique de Louvain, Institute of Mechanics, Materials and Civil Engineering (iMMC), Place du Levant 1, 1348 Louvain-la-Neuve, Belgium

Abstract

This paper presents an anisotropic adaptive strategy for CFD that combines a nearly body-fitted mesh strategy with an iterative anisotropic adaptation to the flow solution. The nearly body-fitted mesh method consists in modeling embedded interfaces by a level-set representation in combination with local anisotropic mesh refinement and mesh adaptation [33]. The generated nearly body fitted meshes are used to perform CFD simulations. Besides, anisotropic mesh adaptation based on the Hessian of the flow solution is used to improve the accuracy of the solution. We show that the method is beneficial in challenging CFD simulations involving complex geometries and time dependent flow, as it suppresses the need for the tedious process of body-fitted mesh generation, without altering the finite element formulation nor the prescription of boundary conditions. The methodology yields accurate flow solutions for a reasonable computational cost, despite very limited user interaction.

Keywords: nearly body-fitted mesh, anisotropic adaptation, embedded interfaces, level-set, CFD, incompressible flow

1. Introduction

Because of the increasingly complex geometries involved in flow problems of industrial relevance, numerical methods based on unstructured meshes have become popular in CFD. However, the corresponding meshing methods require a high-quality CAD description of the geometry, which is not part

[1]Corresponding author. Tel.: +3210472362; Fax: +3210472180.
E-mail address: dieulinh.quan@uclouvain.be

of the traditional workflow in fields like architecture or medicine. Many professionals also lack the expertise required to build appropriate meshes for flow problems. Nevertheless, recent progresses in meshing technology could overcome these barriers.

In this work, we employ anisotropic adaption techniques to generate a nearly body-fitted mesh. The mesh is locally refined depending on a level-set function that describes the geometry without resorting to a CAD model [10, 20]. One of the impressive advantages of the method is that Dirichlet boundary conditions can then be imposed for embedded interfaces in a strong manner by node collocation, just as with classical body-fitted meshes. Unlike other treatments of embedded geometries [14, 21, 3, 15], this technique only requires a standard finite element formulation, without basis enrichment or Lagrange multipliers that alter its numerical properties.

In addition to the adaptation to the geometry, the method presented in this paper involves adaptation to the solution. The adaptation techniques used in this procedure are based on the specification of a metric map [5]: they generate a uniform unit mesh in the prescribed metric space, in order to obtain an anisotropic adapted mesh in the Euclidean space. The metric is thus proportional to the square of the element size to be specified in each direction, that is computed from the level-set function for the adaptation to the geometry, and from the velocity field for the adaptation to the solution. The combination of the implicit description of the geometry and the mesh adaptation to the solution results in a simulation procedure that minimizes the need for user interaction while being computationally efficient.

This paper is organized as follows. In Section 2, we discuss briefly the adaptive strategy for generating a nearly body-fitted mesh which is shown to capture well embedded geometries. Then, the extension of the nearly body-fitted approach to the Navier-Stokes equations is explained in Section 3, where the mesh metric construction for the adaptation to the solution and the metric intersection procedure are described in detail. Section 4 presents numerical computations for some benchmarks cases involving both simple and complex geometries, steady and unsteady cases as well as laminar and turbulent flow regimes. Solutions are then compared with other documented results to demonstrate the accuracy and efficiency of our technique. Finally, conclusions are drawn in Section 5, where some perspectives for future work are also outlined.

2. Adaptive strategy for nearly body-fitted meshes

2.1. "Nearly" body-fitted mesh

This section recalls the general principle of the approach which is discussed in detail by Quan et al. [33]. The basic idea is to generate a mesh that is refined around the embedded geometry, and to impose strong boundary conditions at the nodes that are located closest to the interface, as if the mesh was body-fitted. This *nearly* body-fitted mesh removes the need to modify the finite element kernel for prescribing the boundary conditions on the embedded interface, at the expense of representing the geometry only approximately.

In general, a *nearly* body-fitted mesh is generated as follows:

- The interface known as Γ, which we want to embed in the computational domain, is described by the iso-zero level-set of a signed distance function $\phi(\mathbf{x})$.
- An anisotropic mesh adaptation procedure takes place in the vicinity of Γ, with flat elements stretching along the interface.
- The mesh is split in two by assigning each element e_i to a side of the domain according to the sign of $\phi(\mathbf{c}_i)$, where $\mathbf{c}_i$ is the centroid of the element e_i.

The interface Γ^*, that is composed of the mesh edges separating the two sides of the domain, gives an approximate representation of Γ (see Fig. 2). However, as explained in the following section, the approximation of the geometry and its impact on the finite element solution is very limited if the appropriate level of anisotropic mesh refinement is applied.

2.2. Accuracy in nearly body-fitted mesh approach

Let us first discuss about the geometrical error which is defined as the error in the length of the interface $\mathcal{E}_{geo} = ||l_{\Gamma^*} - l_\Gamma||$ in the academic 2D Laplace problem in a square domain with an embedded planar surface [15]. Consider an initial uniform mesh with element size h_b, and refine this mesh by using isotropic and anisotropic adaptive elements in the vicinity of a horizontal line Γ embedded in the $2D$ square, as can be seen in Fig. 1.

The idealized situation of several element layers at the interface is illustrated in Fig. 2. We denote by AB a finite part of the exact interface Γ.

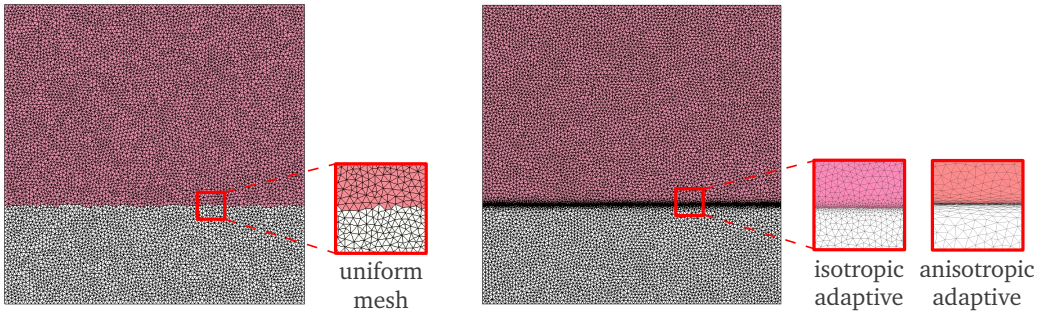

Figure 1: Illustration for uniform and adaptive mesh refinement. The 2D Laplace problem is solved in the colored domain and Dirichlet boundary conditions are applied at the interface between the colored and the white domain.

For simplicity, AB is approximated by a polygonal curve $A_1C_1B_1$ in initial uniform mesh and the geometry error of AB is defined as follows:

$$\mathcal{E}_{geo}^{initial} = \underbrace{A_1C_1 + C_1B_1}_{A_1C_1B_1} - AB = 2h_b - AB \tag{1}$$

We start refining mesh in two approaches, isotropic adaptive (with mesh

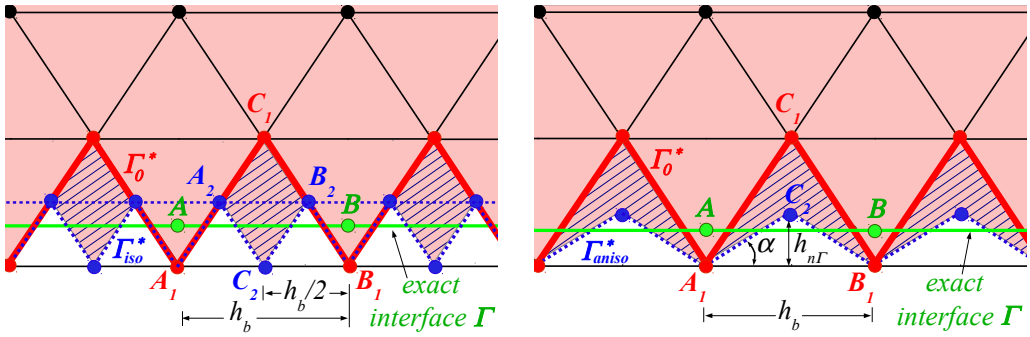

(a) Isotropic adaptive mesh.

(b) Anisotropic adaptive mesh.

Figure 2: Geometry error analysis in isotropic and anisotropic adaptive meshes.

size $h_b/2$) and anisotropic adaptive mesh (mesh size h_b, $h_{n\Gamma}$) in the vicinity of interface Γ as in Fig. 2(a) and Fig. 2(b), respectively. The approximation

of Γ leads to the geometry error:

$$\mathcal{E}_{geo}^{iso} = \underbrace{A_1A_2 + A_2C_2 + C_2B_2 + B_2B_1}_{A_1A_2C_2B_2B_1} - AB = 2h_b - AB \tag{2}$$

$$\mathcal{E}_{geo}^{aniso} = \underbrace{A_1C_2 + C_2B_1}_{A_1C_2B_1} - AB = \frac{h_b}{\cos(\alpha)} - AB \tag{3}$$

Equations (1) and (2) show that although the gap between the exact interface Γ and its approximation Γ^* could be reduced by isotropic adaptive mesh refinement, the geometry error (i.e. the difference between the length of Γ and Γ^*) remains constant. In contrast, the geometry error in anisotropic mesh in Equation (3) depends on $\cos(\alpha)$. Clearly, the smaller the inclined angle α is (i.e. the more anisotropic the element is), the smaller the geometry error. Thus, refining the mesh size $h_{n\Gamma}$ in the direction normal to Γ to a certain level can capture well the embedded geometry. These considerations illustrate the fact that geometry error does not converge in isotropic adaptive mesh refinement, while anisotropic adaptive mesh can recover the optimal order of convergence for $\mathcal{E}_{geo}$.

In order to assess numerically the effect of refinement, we analyze the solution computed on three different refined meshes : a uniformly refined mesh, a locally refined mesh obtained through isotropic adaptation and a locally refined mesh obtained through anisotropic adaptation is carried out to show the efficiency of the method in recovering the optimal rate of convergence for finite elements. All meshes have an equal refinement factor in the bulk $r_b = 2$ but a possibly different refinement factor r_Γ in the vicinity of the interface Γ. The L_2 error $\mathcal{E}_{L_2}$, as well as the geometry error $\mathcal{E}_{geo}$ are computed.

Uniform refinement yields a poor first-order rate of convergence (see in Fig. 3(a)), because the global error is dominated by the approximation of the interface that is of first-order accuracy while an appropriate level of local refinement $r_\Gamma = r_b^{p+1}$ in the vicinity of the interface Γ recovers the optimal convergence rate for the solution, where p is the finite element order.

Although the optimal rate of convergence for the solution is obtained with the isotropically adapted mesh, Fig. 3(b) shows that the geometry error $\mathcal{E}_{geo}$ never converges, even when very fine isotropic elements are used. This is due to the fact that a stair-cased representation of the interface cannot be avoided as explained previously, which may affect particularly the computation of integral quantities on the boundary such as lift and drag in CFD applications.

However, this problem can be circumvented using anisotropic elements. The anisotropic refinement enables the geometrical error to decrease at optimal rate, just like the error on the solution, as seen in Fig. 3(b). In addition, anisotropic adaptive refinement slows down the growth of the number of unknowns, which limits the computational overhead. Results are discussed in detail and more other results for higher order finite elements and 3D examples can be found in [33].

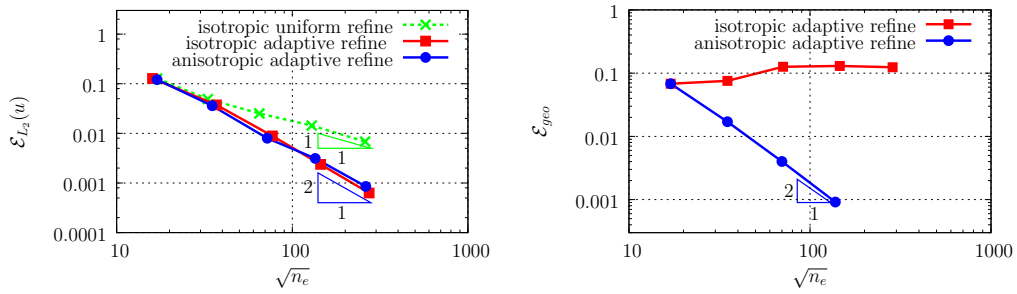

(a) Solution error (b) Geometry error

Figure 3: 2D Laplace problem : error analysis using uniform meshes and adapted meshes.

2.3. Level-set based mesh metric for nearly body-fitted meshes

A good approximation of embedded geometries can be obtained by employing highly anisotropic elements stretching along the interfaces. In this section, we explain how to create such anisotropic meshes in the vicinity of the interface Γ, in a band $\{\mathbf{x} \text{ s.t. } |\phi(\mathbf{x})| \leq E\}$ of thickness $2E$ around Γ. The key aspect of the method is the definition of a metric tensor field that drives the mesh adaptation process by prescribing a direction-dependent mesh size.

An initial isotropic mesh is first created using a standard mesh generation algorithm. At each mesh vertex, the gradient $\nabla\phi(\mathbf{x})$ and the Hessian $\mathcal{H}(\phi(\mathbf{x}))$ of the distance function $\phi(\mathbf{x})$ are computed:

$$\nabla\phi(\mathbf{x}) = \begin{pmatrix} \phi_x \\ \phi_y \\ \phi_z \end{pmatrix}, \qquad \mathcal{H}(\phi(\mathbf{x})) = \begin{pmatrix} \phi_{xx} & \phi_{xy} & \phi_{xz} \\ \phi_{yx} & \phi_{yy} & \phi_{yz} \\ \phi_{zx} & \phi_{zy} & \phi_{zz} \end{pmatrix}. \tag{4}$$

A mesh metric is then build at every mesh vertex as follows:

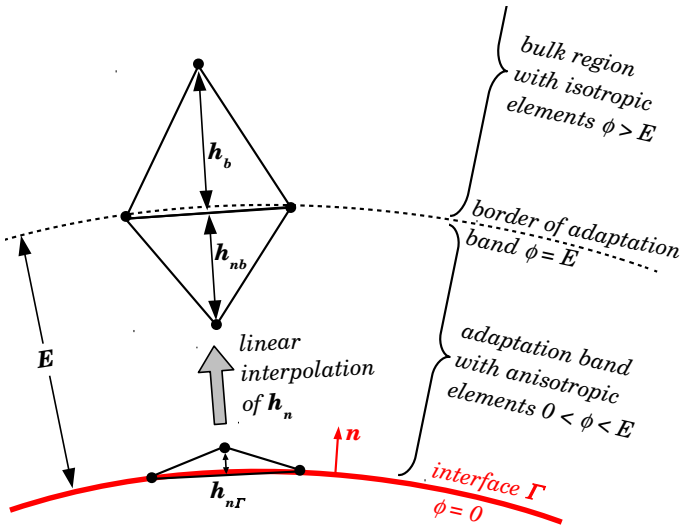

Figure 4: Illustration for mesh generation.

- The unit vectors normal $\mathbf{n}$ and tangent $\mathbf{t_i}$ to Γ, as well as the corresponding curvatures κ_i, are obtained from the gradient $\nabla\phi$ and the Hessian $\mathcal{H}(\phi)$.

- The mesh size h_n to be specified in the normal direction to Γ is computed by a linear interpolation on the distance ϕ between the value $h_{n\Gamma}$ at the interface Γ ($\phi = 0$) and the bulk value h_b at the border of the band ($\phi = E$) (see Fig. 4). The mesh size h_{t_i} to be specified in each tangential direction i to Γ is proportional to the corresponding curvature κ_i.

- The mesh metric $\mathcal{M}_{LS}$ is given by:

$$\mathcal{M}_{LS} = \mathcal{R}^T \begin{pmatrix} \lambda_n & 0 & 0 \\ 0 & \lambda_{t_1} & 0 \\ 0 & 0 & \lambda_{t_2} \end{pmatrix} \mathcal{R}, \tag{5}$$

  where the eigenvalues are computed from the mesh sizes h_n and h_{t_i}

bounded by user-defined minimum h_{min} and maximum h_{max} values:

$$\lambda_n = \min\left(\max\left(\frac{1}{h_n^2}, \frac{1}{h_{max}^2}\right), \frac{1}{h_{min}^2}\right) \tag{6}$$

$$\lambda_{t_i} = \min\left(\max\left(\frac{1}{h_{t_i}^2}, \frac{1}{h_{max}^2}\right), \frac{1}{h_{min}^2}\right) \tag{7}$$

and $R = (\mathbf{n}, \mathbf{t_1}, \mathbf{t_2})^T$.

In the bulk of the domain (i.e. outside the band of thickness $2E$ around Γ), a uniform isotropic element size h_b is prescribed:

$$\mathcal{M}_{LS} = \begin{pmatrix} \frac{1}{h_b^2} & 0 & 0 \\ 0 & \frac{1}{h_b^2} & 0 \\ 0 & 0 & \frac{1}{h_b^2} \end{pmatrix}. \tag{8}$$

The mesh metric $\mathcal{M}_{LS}$ is then passed as input to external anisotropic mesh generator libraries (BAMG in 2D [22] and MMG3D in 3D [13]), that are available in Gmsh [19]. More details about the construction of the metric can be found in [33].

3. Adaptive nearly body-fitted mesh for CFD

The adaptive strategy for CFD combines the nearly body-fitted adaptive mesh approach presented in Section 2 with an iterative anisotropic adaption procedure that is driven by an error estimator based on the Hessian of the flow solution.

3.1. Hessian based mesh metric

Our incompressible Navier-Stokes solver is a stabilized finite element method. Continuous linear ($p = 1$) finite elements are used for interpolating both the velocity $\mathbf{u}$ and the pressure p. The error estimation procedure is based on the norm of the velocity $|\mathbf{u}(\mathbf{x})|$. Because of the $p = 1$ interpolation, the leading term of the discretization error is proportional to the Hessian $\mathcal{H}(|\mathbf{u}(\mathbf{x})|)$ [17].

The Hessian matrix $\mathcal{H}(|\mathbf{u}(\mathbf{x})|)$ contains directional information about the discretization error: it allows us to build a second mesh metric $\mathcal{M}_H = \alpha\mathcal{H}(|\mathbf{u}(\mathbf{x})|)$ that is directly proportional to $\mathcal{H}(|\mathbf{u}(\mathbf{x})|)$ [5, 35]. The factor

of proportionality α between $\mathcal{M}_H$ and $\mathcal{H}(|\mathbf{u}(\mathbf{x})|)$ is not trivial to compute when the aim of the adaptation process is to control the interpolation error. In practice, it is usually more convenient to control the number of elements in the final mesh. In this case, the factor α is easy to compute.

Assume an initial mesh M containing N elements (noted e) on which the Hessian field has been computed. Assume that our aim is to produce an optimized mesh M' with N' elements that respects the anisotropic size field defined by $\mathcal{M}_H$.

Consider an element $e_i \in M$. Assuming that $\mathcal{H}_i$ is the (constant) Hessian in e_i and V_i is the volume (area in 2D) of this element, it is possible to define the non-dimensional volume $V_i^{\mathcal{M}}$ of e_i in the metric space with respect to $\mathcal{H}_i$ as [1]:

$$V_i^{\mathcal{M}} = \sqrt{\det \mathcal{M}_i}\, V_i = \alpha^{d/2} \sqrt{\det \mathcal{H}_i}\, V_i \tag{9}$$

where d is the dimension of the problem. This non-dimensional volume $V_i^{\mathcal{M}}$ represents the number of elements in the region defined by e_i in M'. The number of elements N' in the optimized mesh M' is simply

$$N' = \alpha^{d/2} \sum_{i=1}^{N} \sqrt{\det \mathcal{H}_i}\, V_i \tag{10}$$

The coefficient of proportionality α can then be computed as

$$\alpha = \left(\frac{N'}{\sum_{i=1}^{N} \sqrt{\det \mathcal{H}_i}\, V_i} \right)^{2/d}. \tag{11}$$

3.2. Mesh metric intersection

As at least two metric fields ($\mathcal{M}_{LS}$ and $\mathcal{M}_H$) are constructed, a metric intersection needs be performed in order to provide a single intersected metric to the mesh generator. The intersection operation is based on keeping the most restrictive size constraint among both metrics [1] as well as preserving orientation of the most anisotropic metric.

Fig. 5(a) shows the geometric interpretation for a mesh metric $\mathcal{M}$ associated with an ellipse $\mathcal{E}_M$ in 2D (or ellipsoid in 3D) prescribing at one point the desired element sizes in its principal directions. Consider a point in the vicinity of a 2D embedded geometry where two metrics $\mathcal{M}_{LS}$ and $\mathcal{M}_H$ coexist and the intersection results in $\mathcal{M}_{H \cap LS}$. This means that the two associated ellipses $\mathcal{E}_{LS}$ and $\mathcal{E}_H$ at this point should be intersected in some way to result

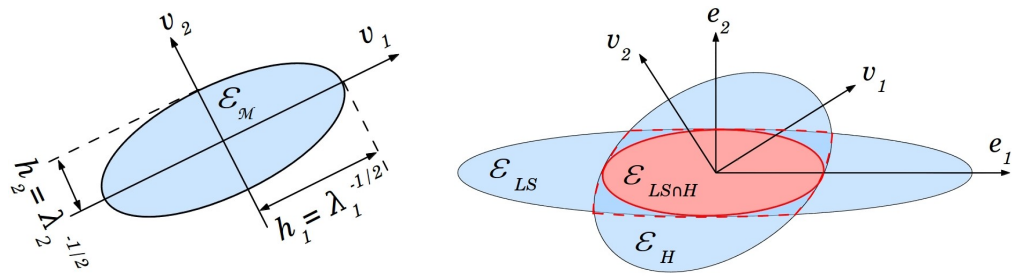

(a) Ellipse representing metric $\mathcal{M}$ (b) Metric intersection $\mathcal{M}_{LS} \cap \mathcal{M}_H$

Figure 5: Geometric interpretation of mesh metric and mesh metric intersection in 2D that preserves the orientation of the most anisotropic mesh metric.

in a single ellipse $\mathcal{E}_{H\cap LS}$. As illustrated in Fig. 5(b), the geometric intersection (dashed line) of both ellipses is not an ellipse itself. Instead, the largest ellipse included in the intersection region, with axes parallel to those of the most anisotropic of both original ellipses (here $\mathcal{E}_{LS}$), is taken as $\mathcal{E}_{LS\cap H}$. Mesh sizes prescribed by $\mathcal{E}_{LS\cap H}$ fulfill the size constraints imposed in both mesh metrics in all directions, while the orientation of the anisotropic elements is preserved.

In practice, the metric intersection procedure can be summarized as follows:

- Eigenvalue decomposition of both $\mathcal{M}_{LS}$ and $\mathcal{M}_H$ to identify the most anisotropic metric, i.e. the metric with the largest ratio of eigenvalues. The basis $\mathcal{R} = \{\mathbf{e_1}, \mathbf{e_2}, \mathbf{e_3}\}$ is retained, with $\mathbf{e_i}$ the normalized eigenvectors of the most anisotropic metric.

- Construction of the intersection metric:

$$\mathcal{M}_{LS\cap H} = \mathcal{R}^T \begin{pmatrix} \max(\mu_1^{LS}, \mu_1^H) & 0 & 0 \\ 0 & \max(\mu_2^{LS}, \mu_2^H) & 0 \\ 0 & 0 & \max(\mu_3^{LS}, \mu_3^H) \end{pmatrix} \mathcal{R}, \tag{12}$$

  where $\mu_i^{LS} = \mathbf{e_i}^T \mathcal{M}_{LS} \mathbf{e_i}$ and $\mu_i^H = \mathbf{e_i}^T \mathcal{M}_H \mathbf{e_i}$.

4. Applications

The overall procedure for CFD problems is illustrated in Fig. 6 and can be explained as follows: in the first step (*step 0*), the problem is solved on initial mesh which is adapted to the level-set only in order to capture the embedded geometry, as there is no information about the flow solution at this time. Next, in intermediate steps (*step* i with $0 < i < N$, N being the total iteration number that we would like to perform), the mesh is successively adapted to both the geometry and flow field using the metric intersection technique presented in Section 3.2. Usually, four iterations ($N = 3$) are sufficient to obtain a final refined mesh that produces a good solution. We note that it is not necessary to impose a high value for the target element number n_H^{target} at the beginning, when the flow resolution obtained from the previous steps is not fine enough: n_H^{target} should be increased step by step. Only the results computed on the final mesh are reported in the paper.

For solving Newtonian fluid flows governed by incompressible Navier-Stokes equations, we use an implicit pressure stabilized finite element method that has been shown to be robust, accurate and stable with linear finite elements ($p = 1$). The details of the spatial discretization scheme can be found in Ref. [28]. The time integration is performed either by a backward Euler scheme or a second-order Diagonally-Implicit Runge-Kutta (DIRK) scheme. The non-linear system of equations arising at each time step is solved by a Newton method that makes use of LU or incomplete LU decomposition algorithms implemented in the PETSc library [2]. For steady cases, the solution is computed by marching in time with increasingly large time steps until the steady state is reached.

In many CFD applications, the wall shear stress is a quantity of engineering or scientific interest. It can be computed directly from the finite element solution by evaluating the velocity gradient of elements adjacent to the wall. In the case of nearly body-fitted meshes however, estimating the wall shear stress in this manner may yield inaccurate results, because of the elements lying on the wall are highly stretched, and they represent only approximately the real geometry. It may thus be beneficial to use the solution further away from the wall than the first layer of elements.

In this work, we compute the wall shear stress through finite differences using values of the flow velocity evaluated at several points in the domain. The procedure is illustrated in Fig. 7. For each boundary edge, the tangential component $u_{t,j}$ of the velocity is evaluated at a series of points P_j along the

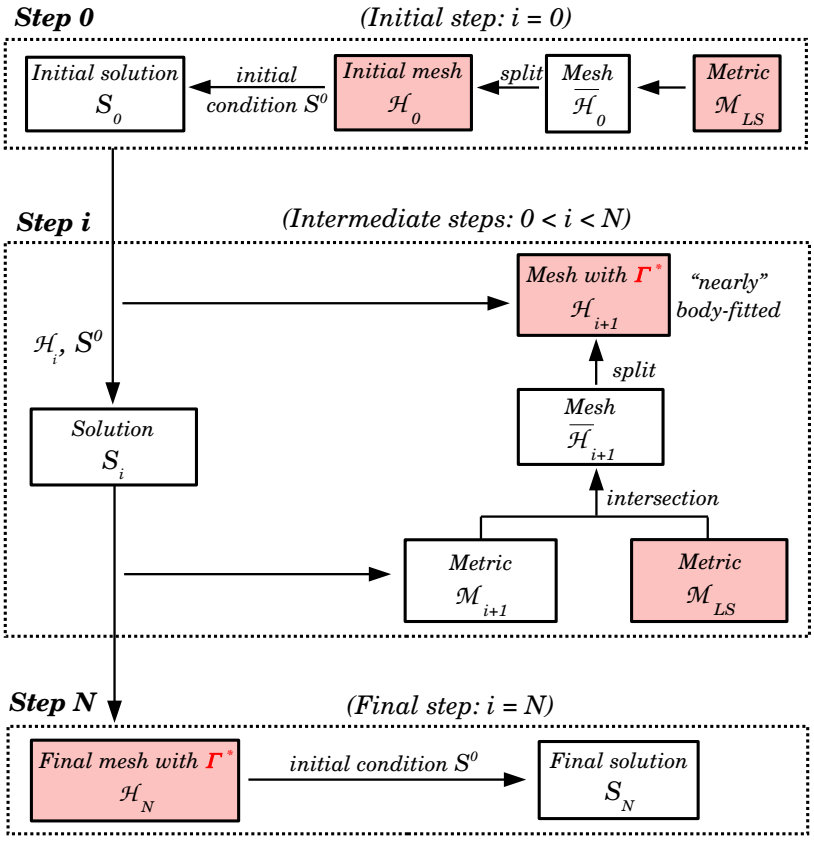

Figure 6: Iterative mesh adaptation to flow solution.

normal direction, starting with the mid-point P_0 of the edge. The points P_j are equally spaced with a step $\Delta n = 0.9 h_{n\Gamma}$, so that the first few points are likely to be located in different elements. Usually, three points P_0, P_1 and P_2 are sufficient to accurately compute the normal gradient of the tangential velocity. We show in this section that this technique results in more accurate wall shear stress predictions than the direct estimation from the finite element solution for most of the applications considered.

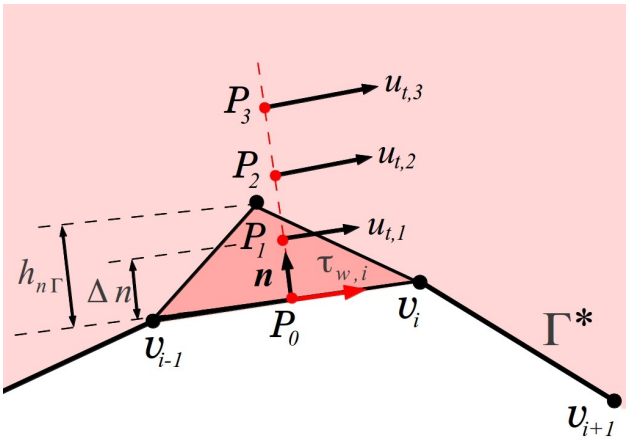

Figure 7: Illustration of tangent velocity derivatives calculation for element e_i on Γ^*.

4.1. Flow over cylinder

In this section, the laminar flow at Reynolds numbers $Re = 20$ and $Re = 40$ is simulated for a two-dimensional circular cylinder immersed in a free-stream and located at the center of the computational domain of size $[15D \times 30D]$. The level-set

$$\phi(x, y) = \sqrt{x^2 + y^2} - R. \tag{13}$$

describes the geometry of the cylinder embedded in the computational domain. Velocity conditions are imposed at the upstream, top and bottom boundaries of the domain, while a pressure condition is imposed on the downstream boundary. The cylinder is subject to a non-slip boundary condition.

The rate of convergence is analyzed considering results at $Re = 20$ computed on five meshes with different levels l of refinement. For the first coarse level ($l = 0$), we define a mesh size in the bulk h_b^0 and the mesh size near the interface in the normal direction $h_{n\Gamma}^0$ as well as a target number n_H^0 of

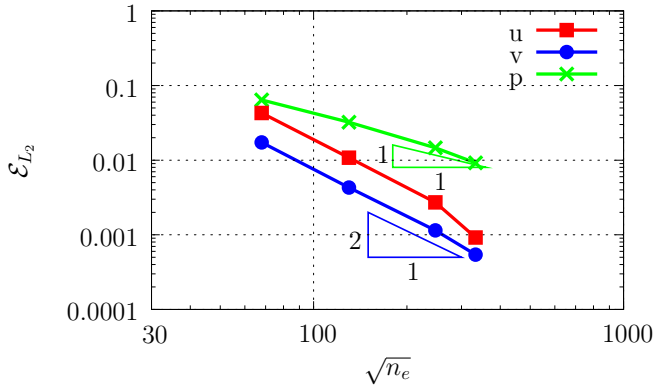

Figure 8: Rate of convergence analysis for flow variables at $Re = 20$

elements generated by the Hessian-based adaptation to the flow. For the next levels, we have :

$$h_b^l = h_b^0 \cdot r_b^l \tag{14}$$
$$h_{n\Gamma}^l = h_{n\Gamma}^0 \cdot (r_b^l)^2 \tag{15}$$
$$n_H^l = n_H^0 \cdot (r_b^l)^2 \tag{16}$$

where $r_b = 2$ is the refinement factor for mesh size in the bulk.

The error norms for the velocities $\mathcal{E}_{L_2}(u)$, $\mathcal{E}_{L_2}(v)$ and for the pressure $\mathcal{E}_{L_2}(p)$ are plotted in Fig. 8. The solution on a the highest refined level ($l = 4$) is considered as the reference solution for computing the error. We can observe the second order accuracy of the method for solving Navier-Stokes equations. Note that the pressure is only first order accurate in our stabilized finite element method.

Table 1 shows mesh statistics in terms of the total number n_e of elements in the mesh, the number n_{LS} of mesh elements resulting from the adaptation to the geometry, as well as the proportion n_{LS}/n_e. The value of n_{LS} is estimated as $n_{LS} = n_{NBF} - n_{iso}$, where n_{iso} is the number of elements in an initial mesh with uniform isotropic element size h_b over the whole domain without embedded interface, and n_{NBF} is the number of elements in the nearly body-fitted mesh resulting from the adaptation to the level-set only.

The drag coefficient C_d and the reattachment length L/D, also shown in Table 1, converge at refinement level $l = 3$ towards a value of 2.15 and 0.92 respectively. At this level, while $n_e - n_{LS} = 108352$ elements are enough

l	h_b	$h_{n\Gamma}$	n_{LS}	n_{LS}/n_e	n_e	C_d	L/D
0	0.8	0.0064	607	13.1%	4607	2.10	0.82
1	0.4	0.0016	717	4.2%	16943	2.15	0.89
2	0.2	0.0004	1380	2.3%	61057	2.15	0.90
3	0.13	0.00016	2630	2.4%	110982	2.15	0.92
4	0.10	0.00010	2935	1.3%	222208	2.14	0.92

Table 1: Mesh statistic for convergence analysis $Re = 20$.

	L/D $Re = 20$	C_d $Re = 20$	L/D $Re = 40$	C_d $Re = 40$
References	[0.73-1.05]	[2.00-2.22]	[1.51-2.59]	[1.48-1.70]
Present	0.92	2.14	2.21	1.58

Table 2: Reattachment length and drag coefficient for steady flow at $Re = 20$ and 40 in comparison with reference results [7, 8, 11, 12, 16, 23, 25, 26, 31, 36, 40, 41, 43, 44]

to capture the physics, only $n_{LS} = 2630$ anisotropic elements are generated for capturing the geometry. The proportion $n_{LS}/n_e = 2.4\%$ shows that the nearly body fitted technique does not imply a significant computational overhead compared to the use of a body-fitted mesh.

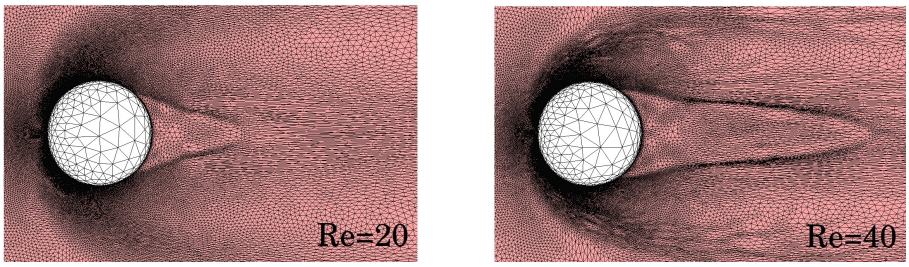

Figure 9: Adaptive mesh in the vicinity of the cylinder for steady case.

The reattachment zone behind the cylinder is observed to be captured well at different Reynolds numbers, as shown in Fig. 9. Both drag and reattachment length in the flow at $Re = 40$ can be seen to converge in Fig. 10. Finally, Table 2 demonstrates that the results for these two quantities are in agreement with reference data from the literature.

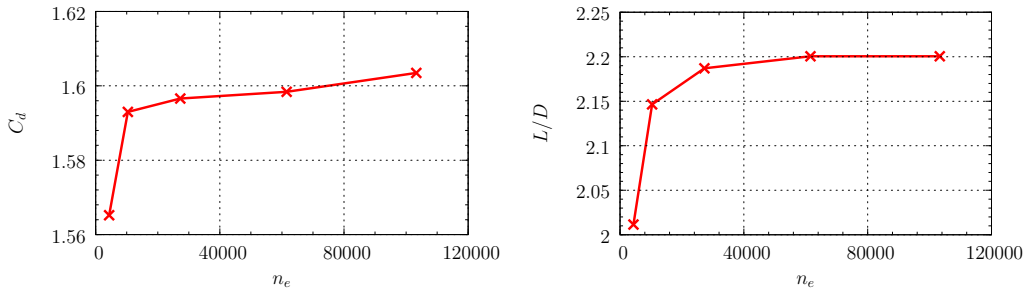

Figure 10: Convergence of drag coefficient and reattachment length at $Re = 40$

4.2. Laminar boundary layer

In this benchmark, a laminar boundary layer on an adiabatic flat plate is computed, the flat plate being immersed in a free stream. The Reynolds number based on the length of the plate is $Re = 20700$, and the numerical solution is compared to the Blasius solution.

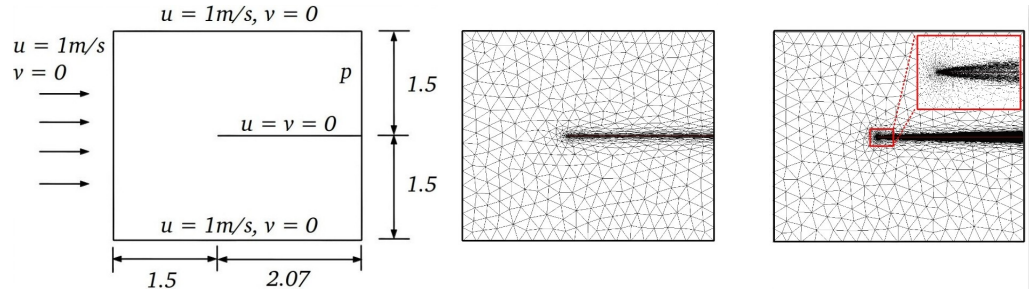

(a) Geometry configuration. (b) Level-set adaptivity. (c) Solution adaptivity.

Figure 11: Illustration for flow over 2D flat plate.

The level-set function in Eq. 17 describes the flat plate embedded in a rectangular domain of size $[-1.5, 2.07] \times [-1.5, 1.5]$. The length of the plate is $L = 2.07$ with the leading edge of the plate is put at the origin $(0, 0)$ and the outlet boundary of the domain is located at the end of the plate. A velocity condition is imposed at the inlet, the upper and the lower boundaries, while the pressure is imposed at the outlet. The plate is subject to a non-slip wall

boundary condition.

$$\phi(x,y) = \begin{cases} \sqrt{x^2+y^2} & \text{if } x < 0 \\ y & \text{elsewhere.} \end{cases} \tag{17}$$

The nearly body-fitted mesh based on the level-set is generated with parameters $h_b = 0.5$ and $h_{n\Gamma} = 0.0001$) and the Hessian-based iterative adaptation to the flow is performed with a target number of elements $n_H = 5000$.

All numerical solutions such as longitudinal velocity u and wall shear stress τ_w are compared with analytical results from the theory of Blasius [38] that considers a self-similar velocity profile. In particular, the exact solution for the wall shear stress $\tau_w(x) = \frac{1}{2}\rho U C_f$ can be determined from:

$$C_f = \frac{0.664}{\sqrt{Re_x}} = 0.664\sqrt{\frac{\mu}{\rho U x}} \tag{18}$$

The adaptation procedure delivers a mesh of n_e = 8,543 elements and a solution that is good agreement with analytical results. The velocity profile is compared in Fig. 12 to results obtained with a body-fitted structured mesh: although the nearly body-fitted mesh contains less elements, it gives a solution of similar accuracy as the body-fitted mesh. Fig. 13(a) shows a plot of the friction coefficient along the plate, while a close-up view for the solution in the region near the leading edge can be observed in Fig. 13(b). The tittles "Blasius-WSS", "FD-WSS" and "FE-WSS" in the plot respectively stand for the Blasius analytical solution, numerical wall shear stress computed directly from the finite element solution and numerical wall shear stress computed by finite difference approach. The results estimated with finite differences provide an improvement compared to the direct evaluation of the velocity gradients from the finite element solution.

4.3. Flow over a NACA0012 airfoil

In this test case, the incompressible laminar flow over an NACA0012 airfoil at $Re = 5000$ and angle of attack $\alpha = 0$ is taken into consideration. For the NACA0012 airfoil, the ratio of the thickness to the chord c is $t = 0.12$ and the leading edge is located at the origin. The coordinates of the airfoil are then defined as:

$$y_B(x) = \pm 5tc\left[0.2969\sqrt{\frac{x}{c}} - 0.1260\left(\frac{x}{c}\right) - 0.3516\left(\frac{x}{c}\right)^2 + 0.2843\left(\frac{x}{c}\right)^3 - 0.1036\left(\frac{x}{c}\right)^4\right] \tag{19}$$

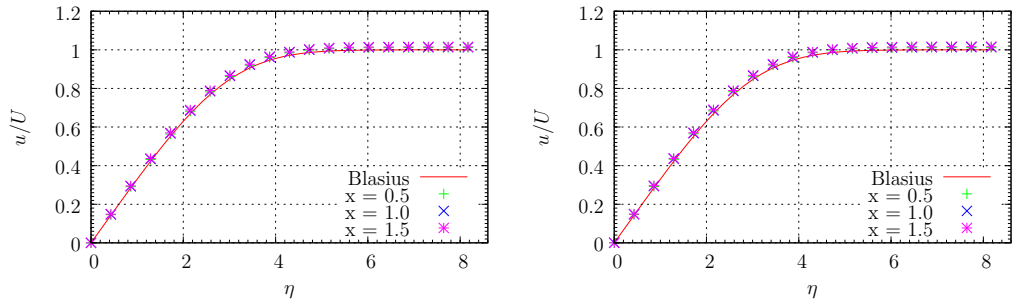

(a) Structured mesh (b) Nearly body-fitted mesh

Figure 12: Velocity profiles u/U using structured and nearly body-fitted meshes for comparison.

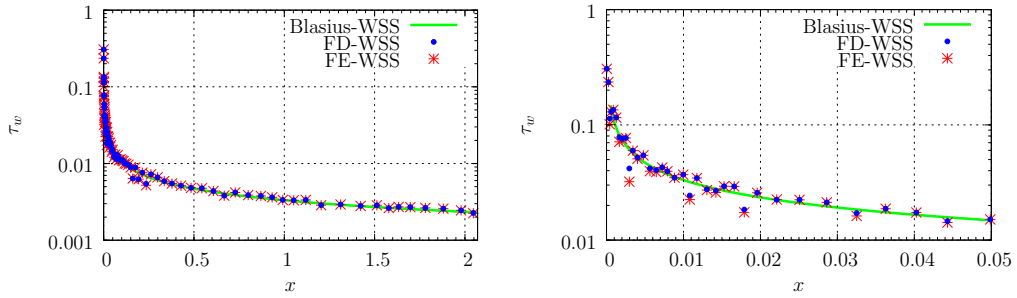

(a) Wall shear stress along the plate (b) Wall shear stress near the leading edge

Figure 13: Analytical and numerical wall shear stress τ_w for comparison.

where the coefficient of the quartic term of the original formula for 4-digit NACA airfoils has been modified in order to obtain a thin trailing edge. The level-set function describing the embedded airfoil geometry for mesh adaptation is the distance to the closest point $(x_P, y_B(x_P))$ located on the airfoil, that is determined numerically:

$$\phi(x,y) = \inf_{x_P \in [0,c]} \sqrt{(x - x_P)^2 + [y - y_B(x_P)]^2}. \tag{20}$$

The mesh resulting from the adaptation procedure, containing $n_e = 27{,}588$ elements ($h_b = 1.5$, $h_{n\Gamma} = 0.0001$), is shown in Fig. 14(a). The results for the pressure coefficient C_p are compared to those obtained on a hybrid body-fitted mesh with $n_e^{BF} = 102{,}000$ elements in Fig. 14(b), showing good agreement. The same comparison for the friction coefficient C_f (Fig. 14(c), 14(d) and 14(e)) is also positive. Again, the benefit of the finite-difference calculation of the wall shear stress over the direct finite-element evaluation for the nearly body-fitted mesh is put in evidence.

Values for the drag and lift coefficients from the adapted mesh are compared in Table 3 to reference data from the literature and results from the body-fitted mesh. A good agreement can be seen with the reference results in terms of drag, particularly with the incompressible solution computed by Beran et al. [4] and the low-Mach number flow simulated by Turkel [42]. Moreover, the location of the separation point near the trailing edge, that is particularly difficult to capture, matches well the result obtained on the body-fitted mesh.

4.4. Flow over an array of cylinders

We present in this section a benchmark involving complex geometry, namely an array of cylinders described in [18]. The incompressible fluid flow through a bank of tubes is simplified as a two-dimensional flow across an array of infinitely long cylinders with porosity $\epsilon = 0.75$. The sample is assumed to have a square shape of size $H \times H$, put in a channel of size $[H \times 4H]$, while the diameter of the cylinders is $D = H/8$. A Dirichlet boundary condition with $u = U_0$ and $v = 0$ is imposed for inlet, top and bottom boundaries while a prescribed constant pressure $p = P_0$ is imposed for the outlet of the computational domain. Surfaces of the cylinders are assumed to be non-slip walls.

The Ergun Reynold number is used for this kind of problem and is de-

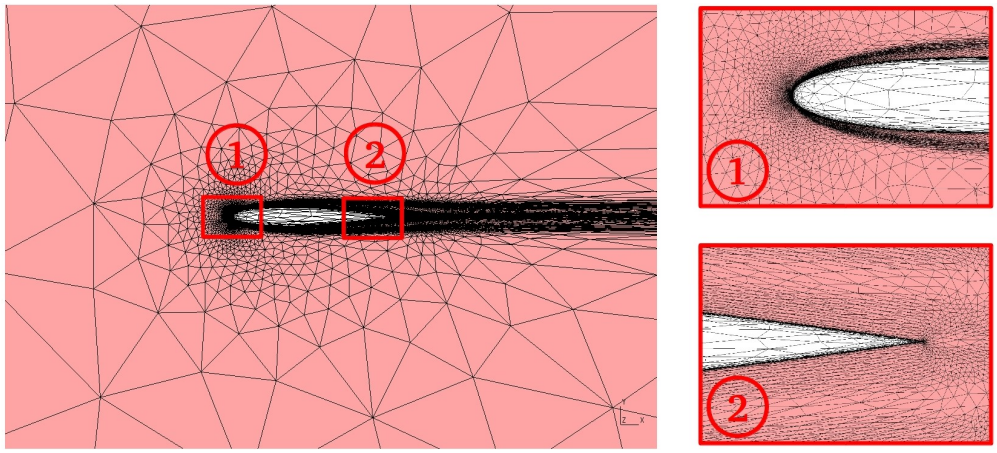

(a) Computational mesh

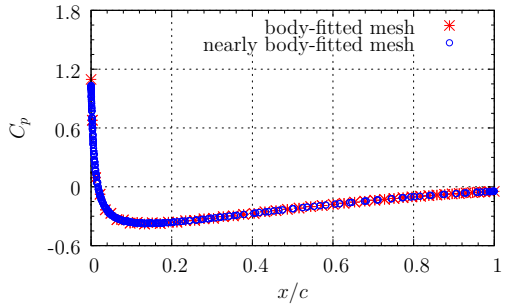

(b) Pressure coefficient along the airfoil.

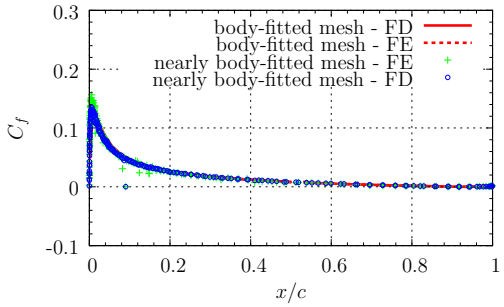

(c) Friction coefficient along the airfoil.

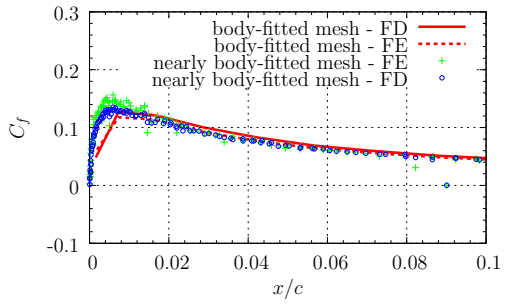

(d) Friction coefficient at the leading edge.

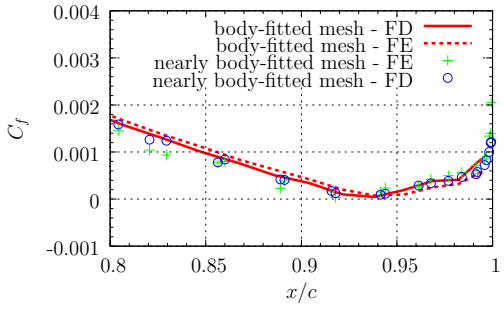

(e) Friction coefficient at the trailing edge.

Figure 14: Incompressible laminar flow over NACA0012 airfoil ($Re = 5000$).

Method	Ma	C_d	C_l	x_{sep}/x_c
Mavriplis[29]	0.5	0.0561	-	0.814
Pagnutti (iso)[30]	0.5	0.0556	0.0095	0.834
Pagnutti (aniso)[30]	0.5	0.0549	0.000114	0.795
Pulliam[32]	0.5	0.0542	-	0.824
Radespiel[34]	0.5	0.0554	-	0.814
Turkel[42]	0.001	0.0516	0.00003	-
Beran[4]	incompressible	0.053	0.0	-
Body-fitted mesh	incompressible	0.0509	0.00020	0.93
Nearly body-fitted mesh	incompressible	0.0513	0.00027	0.925

Table 3: Comparison of drag, lift and separation point for laminar flow over NACA0012 airfoil.

termined based on the porosity ϵ, cylinder diameter D, kinematic viscosity ν and inlet velocity U_0:

$$Re_E = \frac{U_0 D}{\nu(1-\epsilon)} \tag{21}$$

Both steady ($Re_E = 1$) and unsteady flows ($Re_E = 200$) are taken into consideration, the two different configurations being sketched in Fig. 15(a) and 16(a). The distance function in Eq. (22)

$$\sqrt{(x-x_c)^2 + (y-y_c)^2} - R = 0 \tag{22}$$

describes the geometry of a cylinder with centroid (x_c, y_c) embedded inside the domain. Mesh adaptation is performed in the vicinity of all cylinders with mesh sizes $h_{n\Gamma} = 0.0001$, $h_b = 0.5$ in the normal direction to the interfaces and in the far-field region, respectively.

The pressure drop across the system $\Delta p = p_{inlet} - p_{outlet}$ at two vertical positions in the steady case is plotted in Fig. 15(d). The present results are consistent with reference solutions.

As there is a oscillating flow behind cylinder ① at high Reynold number $Re_E = 200$ (see Fig. 16(c)), the lift coefficient C_l, drag coefficient C_d and drag oscillation period T_{ref} are computed in Table 4, demonstrating the accuracy of the method for this kind of complex geometries with less than 5% of with respect to the reference solution.

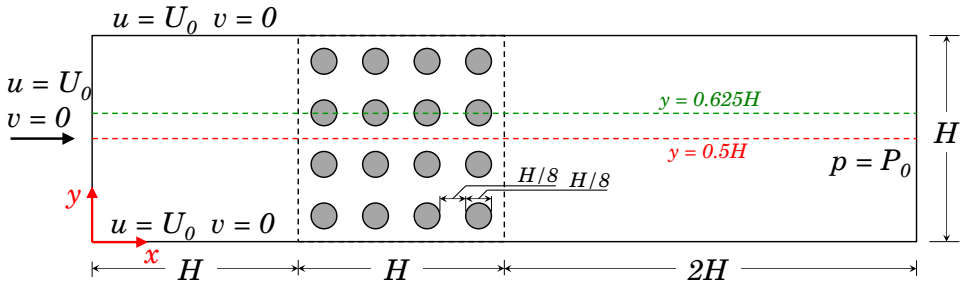

(a) Computational domain and boundary conditions

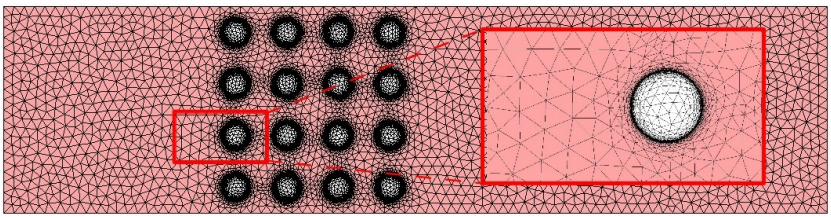

(b) level-set adaptation

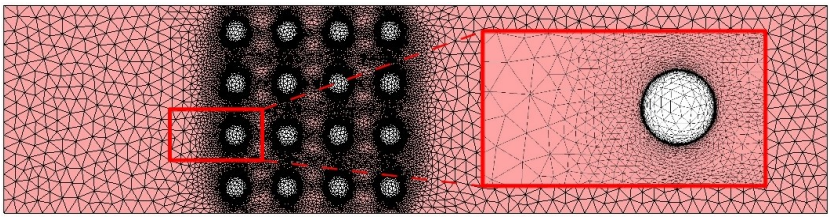

(c) level-set adaptation in combination with solution adaptation

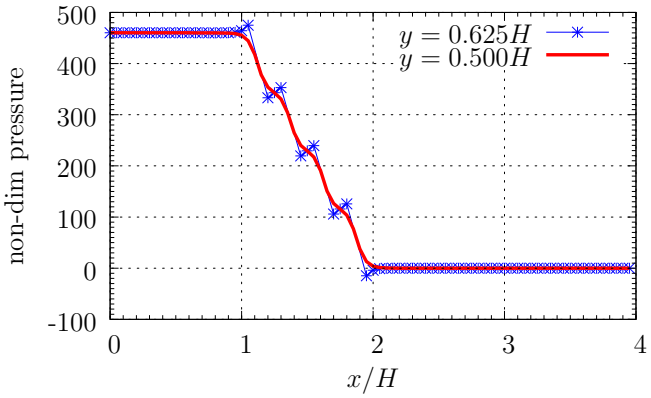

(d) Pressure drop across the system at two vertical positions

Figure 15: Steady flow over multi-cylinders at $Re_E = 1$.

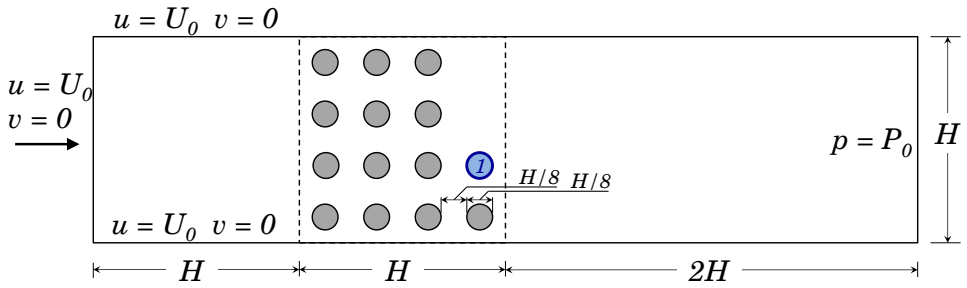

(a) Computational domain and boundary conditions

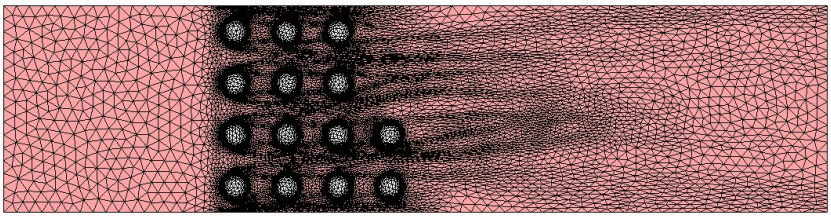

(b) Computational mesh

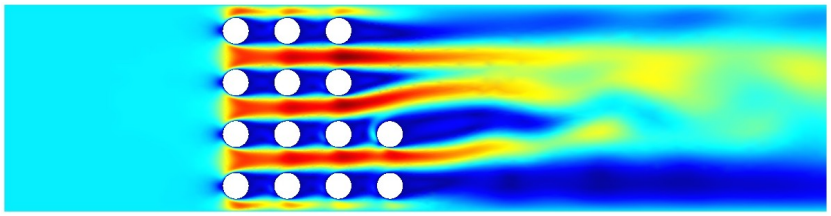

(c) Velocity field

(d) Pressure field

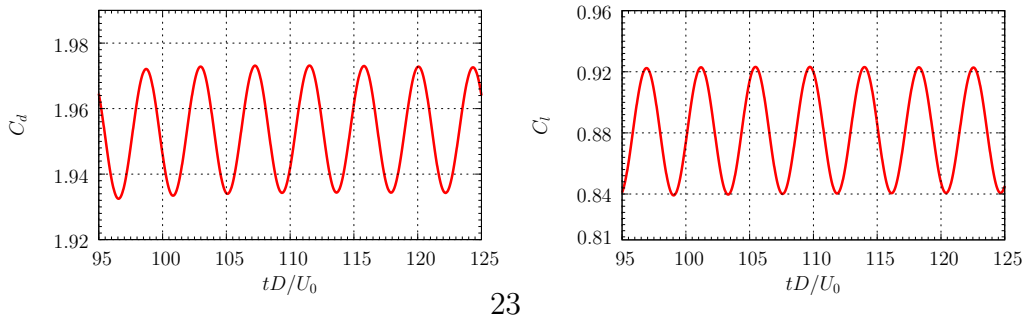

(e) Lift and drag coefficients at $Re_E = 200$

Figure 16: Unsteady flow over multi-cylinders at $Re_E = 200$.

	Geller et al. [18]	Present	Error(%)
C_l	0.915	0.882	3.65%
C_d	2.0548	1.9537	4.92%
TD/U_0	4.2327	4.27	0.88%

Table 4: Comparison of drag, lift and oscillation period ($Re_E = 200$).

4.5. Blood flow in 3D bypass

The last test case consists in a realistic biomedical application, where blood flow simulations are run on a bypassed artery and quantities of biomechanical interest such as the wall shear stress are studied. Blood flow dynamics and arterial wall mechanics are thought to be an important factor in the pathogenesis and treatment of cardiovascular diseases. A number of specific hemodynamic and vascular mechanic factors - notably wall shear stress, pressure and mural stress, flow rate, and residence time - are implicated in aneurysm growth and rupture [6, 39] or in the pathogenesis of atherosclerosis [24].

Most of the current medical imaging techniques allow to extract only the inner wall of the arteries. The outcome of the segmentation procedure is then a triangulation of the surface. This kind of triangulations is however not suited for subsequent numerical simulations, since they are generally oversampled and of very low quality (with poorly shaped and distorted triangles). It is then desirable to modify the initial surface mesh to generate a new surface mesh and as well to create a volume mesh of high quality. During the volume mesh generation, it is furthermore desirable to create a boundary layer mesh that contains enough elements near the wall to capture accurately the wall shear stress.

The approach presented in this paper can be used to circumvent both the complex surface remeshing algorithm and boundary layer mesh generation [27]. In order to obtain a computational mesh for internal flow inside the bypassed aorta, the geometry should be embedded inside a box and the low-quality triangulation is used to define a first level-set ϕ_1. This level-set is computed efficiently (using the Approximate Nearest Neighbour algorithm) as the smallest distance to the triangles of the triangulation. Moreover, two

other plane level-sets are defined by analytical functions:

$$\phi_2(x, y, z) = z + 13.0 \tag{23}$$
$$\phi_3(x, y, z) = z - 10.5 \tag{24}$$

They represent respectively the inlet and outlet boundaries (see Fig. 17(a)). It is necessary to represent these boundaries in order to impose pressure and velocity conditions on them. The surface elements created when splitting the adapted mesh into two domains are then tagged according to the level-set that cuts the corresponding volume element. At the intersection between the wall of the artery and the inlet and outlet boundaries, several level-sets pass through the elements. The first one that cuts an element is chosen to tag the created surface element.

We first create an initial nearly body-fitted mesh base on the level-set ($h_b^0 = 0.3$ and $h_{n\Gamma}^0 = 0.001$) made out of $n_e^{in0} = 147{,}629$ elements for the inner domain. The second mesh containing $n_e^{in1} = 167{,}033$ elements ($h_b^1 = 1.0$, $h_{n\Gamma}^1 = 0.001$) is then generated based on both the level-set and the solution obtained in the first step. Fig. 17(b) and 17(c) show the volume mesh inside the domain in both meshes. The close-up views of the surface mesh at the inlet, stenosis and the bypass-aorta bifurcation in the downstream present a smooth interface embedded in the domain while the two cross-sectional views show that anisotropic adaptive elements capture well the embedded boundary of the 3D model.

First, a geometry error analysis is performed by calculating the absolute geometric deviation of the newly created nodes from the initial triangulation (Hausdorff distance) with the Metro tool [9]. The L_2 error normalized by the diagonal of the bounding box is $4.45 \cdot 10^{-4}$.

Next, the blood flow at Reynold number 500 is simulated. A reference solution is computed on a body-fitted mesh used in Ref. [37] with anisotropic elements of size $h_n^{BF} = 0.025$ in the boundary region ($n_e^{BF} = 178{,}945$). The wall shear stress and velocity profiles are plotted in Fig. 18 for three locations: the bypass, the stenosis and behind the downstream bypass-aorta bifurcation (shown in view 1-1 and 2-2 on Fig. 17(c)). This last region is important to analyse for gaining better understanding of wall thickening and clotting at the interface between the blood and the vessels.

The velocity profiles plotted in Fig. 18(b), 18(d) and 18(f) show a very good agreement between the adapted mesh and the body-fitted mesh, exept a slight difference for the peak velocity. This indicates that the expected flow

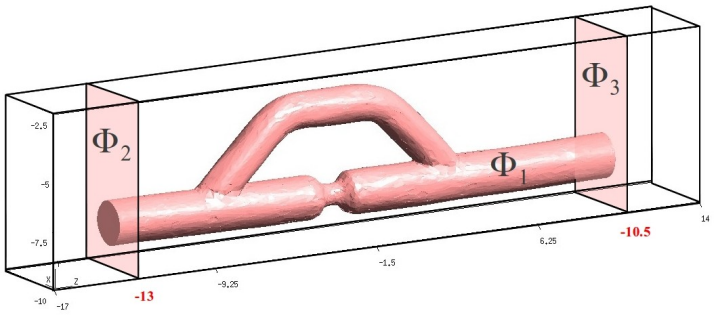

(a) Geometry configuration : 3D bypassed aorta described by level-set Φ_1 and two level-set planes Φ_2, Φ_3 embedded in a box.

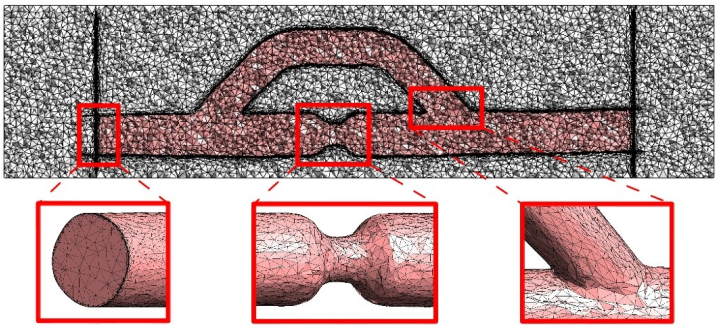

(b) Level-set adaptivity ($h_b = 0.3$, $h_{n\Gamma} = 0.001$, $n_e^{in} = 147,629$): Surface mesh at inlet, stenosis and downstream bifurcation.

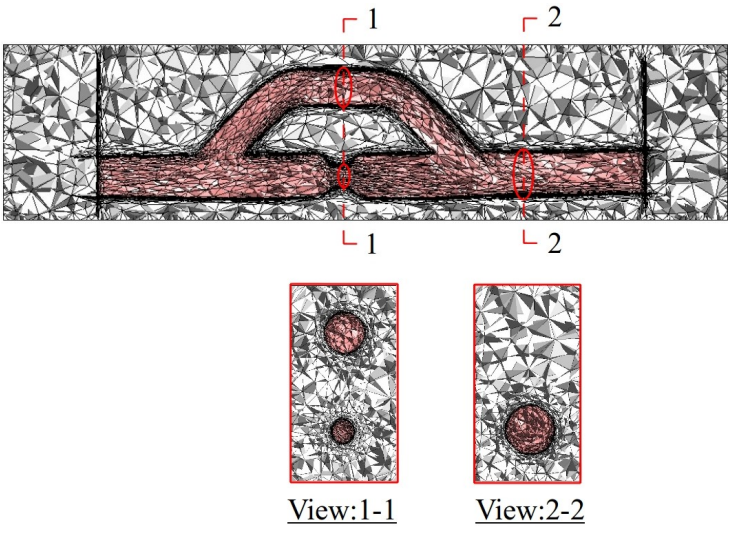

(c) Solution adaptivity ($h_b = 1.0$, $h_{n\Gamma} = 0.001$, $n_e^{in} = 167,033$): Mesh view at two positions $z = -2.5$ and $z = 5.5$.

Figure 17: Computational meshes for a bypass problem.

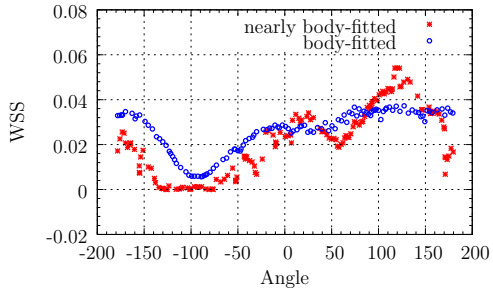

(a) Wall shear stress at bypass (1-1)

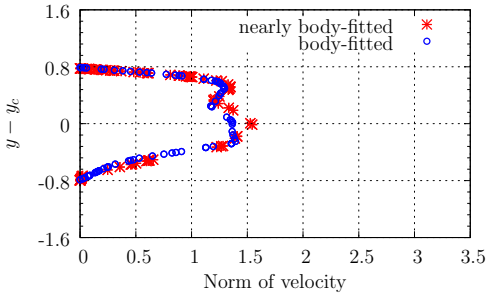

(b) Velocity at bypass (1-1)

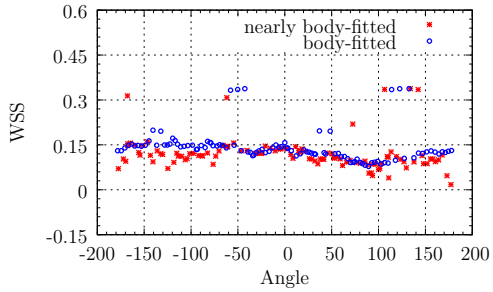

(c) Wall shear stress at stenosis (1-1)

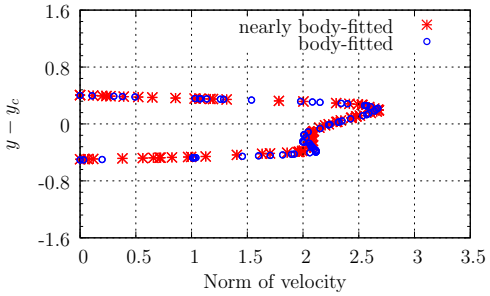

(d) Velocity at stenosis (1-1)

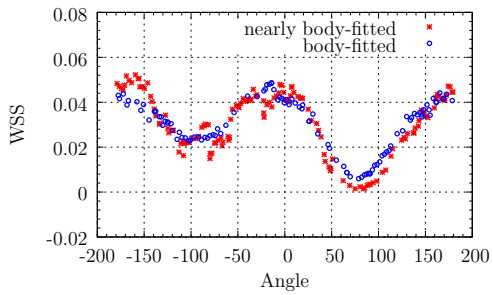

(e) Wall shear stress at downstream (2-2)

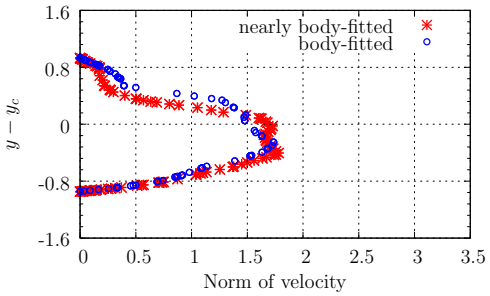

(f) Velocity at downstream (2-2)

Figure 18: Wall shear stress and velocity profiles at bypass, stenosis and downtream of the aorta.

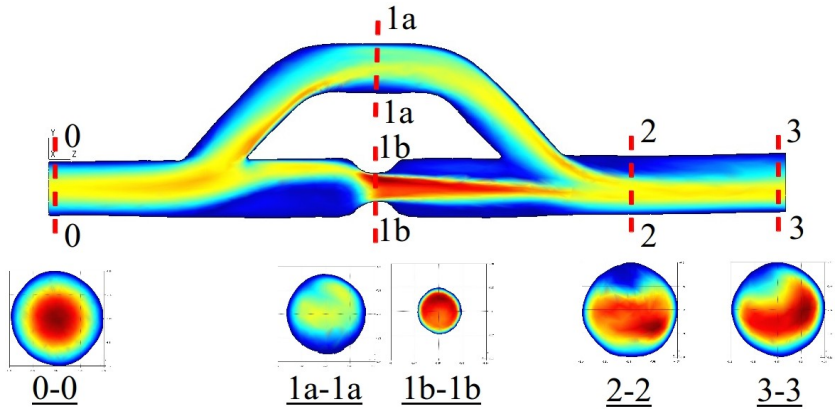

Figure 19: Velocity field over the whole domain and at different positions along the bypassed aorta.

regime is well reproduced. The velocity norm over the whole domain and at different cross sections is presented in Figure 19.

Nevertheless, it can be seen in Plots 18(a), 18(c) and 18(e) that calculating derivative quantities such as the wall shear stress is still challenging in this complex 3D case. Even with the body-fitted mesh, the curves are noisy. However, it seems that the solution obtained with the adapted mesh follows same trends as with the body-fitted mesh in the regions where complex physical phenomena occurs, such as the bypass and the stenosis (cross sections 1-1).

5. Conclusion

In this paper the "nearly body-fitted mesh" approach is successfully extended to the CFD simulations by combining anisotropic adaptation to a level-set with an iterative adaptive procedure driven by the Hessian of the flow solution as error indicator. The advantage of using a nearly body-fitted mesh is to avoid a deep modification in the finite element kernel, while Dirichlet boundary conditions can still be imposed easily on the embedded interfaces in a strong manner by node collocation. Moreover, the adaptation to the solution generates meshes which capture well the behavior of physical phenomena, while improving the computational cost.

The results obtained with several test cases show an optimal rate of convergence in the L_2 norm with linear finite elements ($p = 1$) for the flow variables u and v. Detailed analyses of the flow solution demonstrate that

meshes generated with this approach capture well the flow features. Quantities such as drag, lift, friction and pressure coefficients also converge well and are in a good agreement with reference analytical and numerical results. However, the computation of the wall shear stress requires a special treatment due to the highly stretched shape of the boundary elements and the approximate nature of the geometry representation, which could still be improved.

Overall, we are convinced that this methodology promises a great convenience in solving CFD problems, making it possible to obtain accurate flow solutions at a reasonable cost despite very limited user interaction.

References

[1] F. Alauzet. Size gradation control of anisotropic meshes. *Finite Elements in Analysis and Design*, 46(1-2):181–202, 2010.

[2] S. Balay, J. Brown, K. Buschelman, W. D. Gropp, D. Kaushik, M. G. Knepley, L. Curfman McInnes, B. F. Smith, and H. Zhang. PETSc Web page, 2013. http://www.mcs.anl.gov/petsc.

[3] Helio J.C. Barbosa and Thomas J.R. Hughes. The finite element method with Lagrange multipliers on the boundary: circumventing the Babuska-Brezzi condition. *Computer Methods in Applied Mechanics and Engineering*, 85(1):109–128, 1991.

[4] P. Beran. Steady and unsteady solutions of the Navier-Stokes equations for flows about airfoils at low speeds. *AIAA Paper*, 91-1733, 1991.

[5] H. Borouchaki, P.L. Georges, F. Hecht, P. Laug, and P. Saltel. Delaunay mesh generation governed by metric specifications. part I. algorithms. *Finite Elements in Analysis and Design*, 25(61-83):85–109, 1997.

[6] A. C. Burleson and V. T. Turitto. Identification of quantifiable hemodynamic factors in the assessment of cerebral aneurysm behavior. *Thrombosis and Haemostasis*, 76(118-123), 1996.

[7] D. Calhoun. A Cartesian grid method for solving the two-dimensional streamfunction-vorticity equations in irregular regions. *Journal of Computational Physics*, 176:231–275, 2002.

[8] J.I. Choi, R.C. Oberoi, J.R. Eewards, and J.A. Rosati. An immersed boundary method for complex incompressible flows. *Journal of Computational Physics*, 224:757–784, 2007.

[9] P. Cignoni, C. Rocchini, and R. Scopigno. Metro : Measuring error on simplified surfaces. *Computer Graphics Forum*, 17(2):167–174, 1998.

[10] A. Claisse, V. Ducrot, and P. Frey. Levelsets and anisotropic mesh adaptation. *Discrete and Continuous Dynamical Systems*, 23(1-2):165–183, 2009.

[11] M. Coutanceau and R. Bouard. Experimental determination of the main features of the viscous flow in the wake of a circular cylinder in uniform translation. part 1, steady flow. *Journal of Fluid Mechanics*, 79(2):231–256, 1977.

[12] S.C.R. Dennis and G.-Z. Chang. Numerical solutions for steady flow past a circular cylinder at Reynolds number up to 100. *Journal of Fluid Mechanics*, 42:471–489, 1970.

[13] C. Dobrzynski and P. Frey. Anisotropic Delaunay mesh adaptation for unsteady simulations. *Proceedings of the 17th International Meshing Roundtable*, pages 177–194, 2008.

[14] J.E. Dolbow and L.P. Franca. Residual-free bubbles for embedded Dirichlet problems. *Computer Methods in Applied Mechanics and Engineering*, 197:3751 – 3759, 2008.

[15] J.E. Dolbow and I. Harari. An efficient finite element method for embedded interface problems. *International Journal for Numerical Methods in Engineering*, 78(2):229–252, 2009.

[16] B. Fornberg. A numerical study of steady viscous flow past a circular cylinder. *Journal of Fluid Mechanics*, 98(4):819–855, 1980.

[17] P. Frey and F. Alauzet. Anisotropic mesh adaptation for CFD computations. *Computer Methods in Applied Mechanics and Engineering*, 194(48-49):5068–5082, 2005.

[18] S. Geller, M. Krafczyk, J. Tolke, S. Turek, and J. Hron. Benchmark computations based on lattice-Boltzmann, finite element and finite volume methods for laminar flows. *Computers and Fluids*, 35:888–897, 2005.

[19] C. Geuzaine and J.F. Remacle. Gmsh: A three dimensional finite element mesh generator with built-in pre-and post-processing facilities. *International Journal for Numerical Methods in Engineering*, 79:1309–1331, 2009.

[20] E. Hachem, T. Kloczko, H. Digonnet, and T. Coupez. Stabilized finite element solution to handle complex heat and fluid flows in industrial furnaces using the immersed volume method. *International Journal for Numerical Methods in Fluids*, 68(1):99–121, 2012.

[21] M. Hautefeuille, C. Annavarapu, and J.E. Dolbow. Robust imposition of Dirichlet boundary conditions on embedded surfaces. *International Journal for Numerical Methods in Engineering*, 90(1):40–64, 2011.

[22] F. Hecht. Bamg: Bidimensional anisotropic mesh generator, 2006. http://www.freefem.org/ff++.

[23] F. Ilinca and J.-F. Hétu. A finite element immersed boundary method for fluid flow around rigid objects. *International Journal for Numerical Methods in Fluids*, 65:856–875, 2011.

[24] R. Krams, J.J. Wentzel, J.A.F. Oomen, R. Vinke, J.C.H. Schuurbiers, P.J. de Feyter, P.W. Serruys, and C.J. Slager. Evaluation of endothelial shear stress and 3D geometry as factors determining the development of atherosclerosis and remodeling in human coronary arteries in vivo. *Arteriosclerosis, Thrombosis, and Vascular Biology*, 17:2061–2065, 1997.

[25] D.-V. Le, B.-C. Khoo, and K.-M. Lim. An implicit-forcing immersed boundary method for simulating viscous flows in irregular domains. *Journal of Computer Methods in Applied Mechanics and Engineering*, 197:2119–2130, 2008.

[26] A.L.F. Lima E. Silva, A. Silveira-Neto, and J.J.R Damasceno. Numerical simulation of two-dimensional flows over a circular cylinder using the immersed boundary method. *Journal of Computational Physics*, 189:351–370, 2003.

[27] E. Marchandise, P. Crosetto, C. Geuzaine, J.-F. Remacle, and E. Sauvage. *Quality open source mesh generation for cardiovascular flow simulations*, volume accepted of *Springer Series on Modeling, Simulation and Applications*, chapter of modelling physiological flows. Springer-Verlag, Berlin Heidelberg, 2011.

[28] E. Marchandise and J.-F. Remacle. A stabilized finite element method using a discontinous level set approach for solving two phase incompressible flows. *Journal of Computational Physics*, 219(2):780–800, 2006.

[29] D. Mavriplis and A. Jameson. Multigrid solution of the two-dimensional Euler equations on unstructured triangular meshes. *AIAA paper*, 87-0353, 1987.

[30] D. Pagnutti and C. Ollivier-Gooch. Delaunay-based anisotropic mesh adaptation. *Engineering with Computers*, 26:407–4185, 2010.

[31] J. Park, K. Kwon, and Choi H. Numerical solutions of flow past a circular cylinder at Reynolds numbers up to 160. *KSME International Journal*, 12(6):1200–1205, 1998.

[32] T.H. Pulliam. Efficient solution methods for the Navier-Stokes equations, 1985.

[33] D.-L. Quan, T. Toulorge, E. Marchandise, J.-F. Remacle, and G. Bricteux. Anisotropic mesh adaptation with optimal convergence for finite elements using embedded geometries. *Computer Methods in Applied Mechanics and Engineering*, 268:65–81, 2014.

[34] R. Radespiel. A cell-vertex multigrid method for the Navier-Stokes equations. *NASA TM-101557*, 1987.

[35] J.-F. Remacle, X. Li, N. Chevaugeon, and M.S Shephard. Transient mesh adaptation using conforming and non conforming mesh modifications. In Sandia National Laboratories, editor, *Proceedings, 11th International Meshing Roundtable*, September 15-18 2002.

[36] D. Russell and Z.-J. Wang. A Cartesian grid method for modeling multiple moving objects in 2D incompressible viscous flow. *Journal of Computational Physics*, 191:177–205, 2003.

[37] E. Sauvage, J.-F. Remacle, and E. Marchandise. Anisotropic curvature-based mesh adaptation with applications to blood flow. *Submitted to Engineering with Computers*, 2013.

[38] H. Schlichting. *Boundary layer theory*. McGraw-Hill Book Company, Inc., 1960.

[39] A. M. Shaaban and A.J. Duerinckx. Wall shear stress and early atherosclerosis. *American Journal of Roentgenology*, 174:1657–1665, 2000.

[40] D. Sucker and H. Brauer. Fluiddynamik bei quer angestromten zylindern. *Warme- und Stoffubertragung*, 8:149–158, 1975.

[41] D.-J. Tritton. Experiments on the flow past a circular cylinder at low Reynolds numbers. *Journal of Fluid Mechanics*, 6(4):547–567, 1959.

[42] E. Turkel, R. Radespiel, and N. Kroll. Assessment of preconditioning methods for multidimensional aerodynamics. *Computers & Fluids*, 26(6):613–634, 1997.

[43] C. Wieselsberger. New data on the laws of fluid resistance. *NACA TN 84*, 1922.

[44] T. Ye. An accurate Cartesian grid method for viscous incomressible flows with complex immersed boundary. *Journal of Computational Physics*, 156:209–240, 1999.